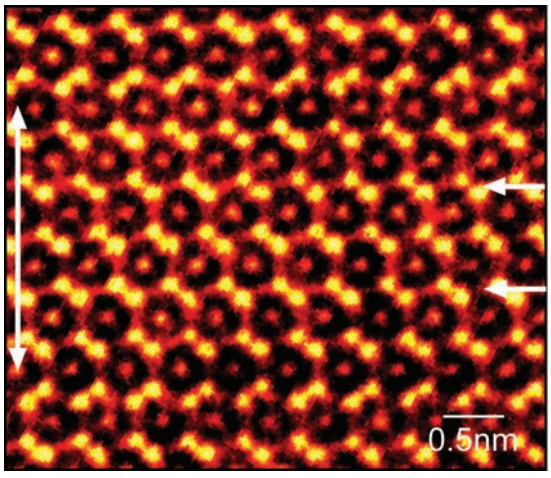

Fig. 4. A Z-contrast image of the <11-20> projection of a faulted region of the C14 variant of the Cr_2Hf Laves phase. This region (between the double arrow on the left) has the C15 cubic structure and could be formed by stacking faults in the C14 structure (indicated by the two short arrows on the right) that result from the passage of two synchro-Shockley dislocations.

kinetics of all four of these processes is controlled by the mobility of synchro-Shockley dislocations. Much understanding could be gained from atomistic simulations of the motion of this type of dislocation. Understanding the structure of the dislocation core and its influence on the ability of Laves phases to deform is central to designing alloys with optimized mechanical properties. In addition, these concepts can be extended to other crystal structures where the slip planes have more than one spacing.

References and Notes

1. J. P. Hirth, J. Lothe, *Theory of Dislocations* (McGraw-Hill Series in Materials Science and Engineering, McGraw-Hill, New York, 1968).
2. F. Laves, H. Witte, *Metallwirtsch. Metallwiss. Metalltech.* **15**, 840 (1936).
3. J. D. Livingston, *Phys. Status Solidi A* **131**, 415 (1992).
4. C. W. Allen, P. Delavignette, S. Amelinckx, *Phys. Status Solidi A* **9**, 237 (1972).
5. Y. Liu, J. D. Livingston, S. M. Allen, *Metall. Mater. Trans. A* **23**, 3303 (1992).
6. K. S. Kumar, D. B. Miracle, *Intermetallics* **2**, 257 (1994).
7. Y. Liu, J. D. Livingston, S. M. Allen, *Met. Mat. Tran. A* **26**, 1441 (1995).
8. Y. Kitano, Y. Komura, H. Kajiwara, E. Watanabe, *Acta Crystallogr. A* **36**, 16 (1980).
9. P. M. Hazzledine, P. Pirouz, *Scripta Metall. Mater.* **28**, 1277 (1993).
10. C. S. Barrett, T. B. Massalski, *Structure of Metals: Crystallographic Methods, Principles, and Data,* vol. 35 of International Series on Materials Science and Technology (Pergamon, Oxford, ed. 3,1987).
11. K. Husimi, *Prog. Theor. Phys.* **5**, 177 (1950).
12. P. D. Nellist, S. J. Pennycook, *Phys. Rev. Lett.* **81**, 4156 (1998).
13. P. D. Nellist *et al.*, *Science* **305**, 1741 (2004).
14. M. L. Kronberg, *Acta Metall.* **5**, 507 (1957).
15. J. B. Bilde-Sørensen *et al.*, *Acta Mater.* **44**, 2145 (1996).
16. P. Pirouz *et al.*, *Acta Mater.* **44**, 2153 (1996).
17. T. Geipel *et al.*, *Acta Mater.* **44**, 2165 (1996).

18. This research was sponsored by the Office of Basic Energy Sciences, U.S. Department of Energy at Oak Ridge National Laboratory, under contract no. DE-AC05-00OR22725. S.K. acknowledges the support from the NSF-sponsored Materials Research Science and Engineering Center on Micro- and Nano-Mechanics of Materials at Brown University (contract no. DMR-9632524), and P.H. acknowledges support from U.S. Air Force Research Laboratory contract no. F33615-01-5214 with UES, Incorporated.

4 October 2004; accepted 22 December 2004
10.1126/science.1105962

End States in One-Dimensional Atom Chains

J. N. Crain* and D. T. Pierce

End states—the zero-dimensional analogs of the two-dimensional states that occur at a crystal surface—were observed at the ends of one-dimensional atom chains that were self-assembled by depositing gold on the vicinal Si(553) surface. Scanning tunneling spectroscopy measurements of the differential conductance along the chains revealed quantized states in isolated segments with differentiated states forming over end atoms. A comparison to a tight-binding model demonstrated how the formation of electronic end states transforms the density of states and the energy levels within the chains.

The break in translational symmetry at a crystal surface creates surface electronic properties that differ from those in the bulk crystal and localize at the surface layer (*1*, *2*). The formation of surface states and resonances is a general property of solid surfaces, and the delicate interplay between the surface electronic structure and the atomic positions often leads to complex surface reconstructions in which the atoms in the top layer rearrange to minimize the surface energy.

In analogy to the surface of a bulk solid, we expect to observe similar physics in reduced dimensions at the edge or end of a nanostructure. Similar to a two-dimensional (2D) surface state formed at the surface of a bulk sample, an edge or step in a 2D structure breaks the 2D symmetry and can form a 1D edge state (*3*). Likewise, a finite 1D chain of atoms should exhibit zero-dimensional end states at its termini. An end state requires two criteria: (i) The wave function of the state must be localized to the end atoms, and (ii) it must decay exponentially into the chain (*2*). Scanning tunneling microscopy (STM) and scanning tunneling spectroscopy (STS) enable the spatial mapping of differentiated electronic structure within a nanostructure. Thus, the local density of states (DOS) can be mapped in real space, providing direct access to electronic edge or end effects. Furthermore, questions of the spatial variation of the wave function away from the end of a 1D structure can be answered directly.

So far, definitive spectroscopic evidence for the existence of end states in 1D structures has been lacking. Research has instead focused on the quantum mechanics of electrons confined to reduced dimensions within the surface layer. Electrons are partially reflected by step edges on metal surfaces and can exhibit refraction at the interface between two media (*4*–*7*). Electrons also exhibit quantum confinement when trapped within atomic "corrals" assembled by STM (*8*). At the 1D limit, finite atomic chains of Au on NiAl(110) (*9*, *10*) and Cu on Cu(111) (*11*) constructed by STM exhibit quantized electronic states, and the observation of spectroscopic enhancement at or near the ends of these chains suggested the possibility of the formation of end states. However, the weakness of these effects in the systems studied, compounded with the possibility of experimental artifacts (*10*, *11*), precluded unequivocal assignment. In the Si(553)-Au atom chains described below, end states are unequivocally manifested through a marked transfer of the DOS from the empty to the filled states above the end atoms. Furthermore, we found that quantized states within finite chains can no longer be described by a particle-in-a-box model, which has been successful in the previous studies (*9*–*11*), but rather require a model that includes end states.

To fabricate 1D chains, we used the self-assembly of chain reconstructions on stepped

Electron Physics Group, National Institute of Standards and Technology, Gaithersburg, MD 20899–8412, USA.

*To whom correspondence should be addressed. E-mail: jason.crain@nist.gov

Si templates driven by the deposition of gold at elevated temperatures (*12*). Gold chain reconstructions on stepped Si have been studied extensively with angle-resolved photoemission (*12*–*16*). Because photoemission gives spatially averaged electronic properties, to date the role of individual defects has remained largely unexplored (*17*, *18*). Here, we focus on Si(553)-Au, which exhibits several metallic bands with 1D dispersion (*19*) and has few defects. In this case, the defects appear as dark voids in STM images (Fig. 1) that leave isolated segments with chain lengths that vary depending on the defect density. All of the measurements were made at room temperature, higher than the temperatures at which charge density wave transitions have been observed in similar 1D chains on Si (*20*, *21*). Such transitions transform the electronic structure from metallic to insulating, so a room-temperature study is desirable to access the chains in their metallic phase.

The formation of end states in finite chain segments is already apparent from comparing STM images of the same sample region taken at opposite polarity (Fig. 1). At a sample bias of +0.5 V (Fig. 1, A, C, and E), the chains appear shorter than at a bias of –1 V (Fig. 1, B, D, and F). This apparent change in length is caused by a contrast reversal over the end atoms, as is apparent from an enlargement of a nine-atom chain (Fig. 1, C and D) and from topography line profiles along the chain (Fig. 1, E and F). At positive bias the end atoms are hardly visible and the atoms second from the end are enhanced, whereas at negative bias the end atoms are enhanced. Such a polarity contrast in STM indicates an underlying difference in the DOS for the empty and filled states near the ends of the chains. On the end atoms, the DOS is transferred from the empty to the filled states.

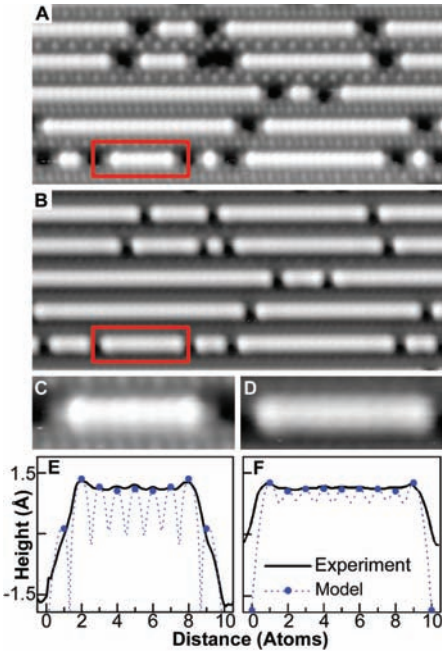

Fig. 1. The effects of end states are visible by comparing STM constant-current mode (0.1 nA) images of the same area (8 by 19 nm) of Si(553)-Au at positive and negative sample biases. The chains appear shorter at +0.5-V sample bias (**A**) than at –1-V sample bias (**B**). The areas inside the red boxes in (A) and (B) are expanded to show an enlargement of a nine-atom chain in (**C**) and (**D**), respectively, and line profiles of the topography along the chain are compared with a tight-binding model in (**E**) and (**F**). The end atoms are barely visible at +0.5 V [(C) and (E)] but are enhanced at –1 V [(D) and (F)].

The differential conductivity as measured by STS provides a direct measure of the local DOS at the tip position and thus allows a detailed study of the electronic variation near the ends of a chain. Figure 2 shows an example for a seven-atom chain with spectra taken beyond the end of the chain, over an end atom, and on an interior atom. Beyond the end of the chain, there is a clear gap with little intensity near the Fermi energy (E_F) (Fig. 2B, green). The boundaries of the gap are consistent with the measured valence-band maximum for Si(553)-Au, –0.3 eV, from photoemission (*12*) and the 1.1-eV band gap of Si. Over the end atom, the differential conductance exhibits a new peak at –0.75 V (Fig. 2B, red). In contrast, the interior atom (Fig. 2B, blue) has an additional peak at +0.5 V inside the band gap.

Spectroscopy along the chains further revealed quantized electronic states that are confined within the isolated chain segments. An isolated atom displays a single state at –0.75 V, which splits into two states at –0.75 and –0.45 V for a two-atom dimer (Fig. 2, C and D). This split is the expected hybridization for a dimer, although the splitting between the states is smaller than in previous studies (*9*–*11*). To best distinguish the two states, we compared spectra from the center and edge of the dimer (Fig. 2D, red). At the center, the state at –0.75 V is clearly seen but the state at –0.45 V appears only as a shoulder. Over the edge of the dimer, although the intensity is low, the –0.75-V peak is absent and allows clear resolution of the –0.45-V state.

In contrast, the three-atom chain exhibits a new peak that is nearly 1 eV higher in energy and is confined to the central atom. This apparent departure for the three-atom chain is attributable to end states, which are characteristic of chains three atoms or more in length. The empty state 0.5 eV above E_F lies in the gap of the Si substrate (Fig. 2B), but states below –0.3 eV are degenerate with the Si bulk bands and are thus technically "end resonances," analogous to the distinction between states and resonances at surfaces of bulk solids.

To elucidate these end effects, we performed spectroscopy in a dense line of points along three-, four-, and five-atom chains (Fig. 3, D, F, and H). These conductance images are formed from individual conductance spectra like those in Fig. 2, B and D, taken at each point along the atom chain. Each spectrum is divided by a second-order polynomial, which approximately removes the transmission function, to allow a more accurate comparison with the theoretical DOS (*22*). This procedure maps spatial variations in the DOS along the chains (*23*). For example, the states seen in the individual spectra for the three-atom chain in Fig. 2D (blue) are mapped in Fig. 3D. The state at +0.5 V (blue circles in Fig. 2D) appears as a dot that is localized to the central atom (position 2 in Fig. 3D). In contrast, the state at –0.7 V (blue triangles in Fig. 2D) has the highest intensity over the end atoms at positions 1 and 3, with lower intensity in the middle. States in the upper corners (>0.8 V) are localized to the regions

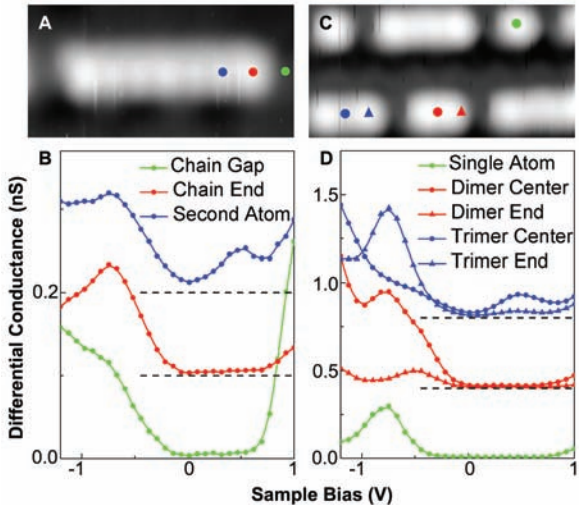

Fig. 2. On the left (**A**), an STM topography image shows a seven-atom chain with (**B**) selected spectra taken in the region beyond the chain (green), over an end atom (red), and over an atom second from the end (blue). On the right (**C**), an STM topography image shows several chains ranging in length from one to four atoms. (**D**) Spectroscopy shows one state for an isolated atom that splits into two states for a dimer, as is expected from the atomic hybridization. The three-atom chain shows a new positive state that is much higher in energy and is localized over the middle atom. The image sizes are (A) 2 by 4 nm and (C) 2.5 by 5 nm. The set point voltages are –1.2 V for (A) and (B) and –0.7 V for (C) and (D). Spectroscopy curves are offset by 0.1 nS in (B) and 0.4 nS in (D) for ease of display and offset baselines for each are also included.

beyond the chain ends and are attributable to either (i) the onset of the conduction band or (ii) empty defect states. The apparent high intensity beyond the ends of the chains is misleading because of the marked inward motion of the tip (>1 Å) that leads to an exponential increase in the differential conductivity (*23*).

To interpret the DOS, we use a tight-binding model in which we consider the states in the chains as atomic wave functions, approximated as a Gaussian at each site, interacting in one dimension. The hopping integral between the wave functions leads to the formation of hybridized states that are a mixture of the atomic wave functions, similar to hybridized states in a molecule. The resulting chain wave functions and eigenenergies are parameterized in terms of the hopping integrals and the binding energies at each atomic site, with the hopping integrals determining the bandwidth and the shape of the band for an infinite chain. The advantage of the tight-binding approach is that it allows differentiation of states at the end atoms. By shifting the electron binding energy on atoms at the ends of the chain relative to the interior atoms, we can model the formation of end states.

A comparison of the DOS for a three-atom chain from the tight-binding calculation (Fig. 3, A, B, and C) and experiment (Fig. 3D) provides the simplest demonstration of the electronic end effects. First, consider the chain without including the end states and with only the nearest-neighbor hopping integral, t_1 = –0.35 eV (Fig. 3A) (*24*). The electronic binding energy determines the energy zero, and the result is similar to a particle in a simple-square well potential with a tight-binding dispersion relation (*11*). The n = 1, 2, and 3 quantum well states have evenly spaced energies and exhibit one, two, and three peaks in the DOS along the chains, respectively. This result contrasts with the experimental data, which has only two resolved states with very different topology (Fig. 3D). The empty states are missing intensity over the end atoms, whereas the filled states have high intensity over the end atoms. Assuming the total DOS at each atomic position is conserved, this result implies a transfer of DOS from the empty to the filled states. Adding a large positive second-nearest-neighbor hopping integral, t_2 = 0.2 eV, to the model effectively lowers the energy of the n = 2 state so it is nearly degenerate with n = 1 (Fig. 3B) but cannot explain the redistribution of DOS over the end atoms. For Fig. 3C, we used different binding energies for the end and interior atoms of –0.6 and 0.27 eV, respectively, with t_1 = –0.19 eV and t_2 = 0.1 eV, which provides the best agreement with the experimental data. The n = 1 and n = 2 states are nearly degenerate and have enhanced DOS over the end atoms. The resulting redistribution of DOS matches qualitatively the DOS in the experiment and explains why only two states are resolved (Fig. 3D). Thus, we can directly attribute the redistribution of DOS to the electronic end effects. In an alternative representation, the transfer of DOS implies a transfer of charge from the interior to the end atoms.

Spectroscopy of longer chains shows similar end states, as is seen for four- and five-atom chains (Fig. 3, E to H). In both cases, the transfer of DOS over the end atoms is similar to that for the three-atom chain, with almost no intensity for the empty states and an accumulation of intensity for the filled states in the range of –0.6 to –0.8 V. Furthermore, similar end states were formed for longer chains (*25*). A tight-binding model with the same few parameters provides a consistent, semiquantitative description of the experimental data for chain lengths ranging from four to nine atoms (*26*). If the model is extended to a semi-infinite chain, the parameters we derived, with binding energy shift $\varepsilon_1 - \varepsilon_0$ = –0.33 eV at the end atom that is comparable to the hopping integral t_1 = –0.34 eV, are consistent with the formation of a localized end state (*2*). The inclusion of second-atom terms in the binding energy shift suggests electronic end effects that extend at least two atoms into the chain. STM topography data from Fig. 1 reflect this assertion and show a clear enhancement of the second atom at positive bias that corresponds to the increased binding energy of the second atoms in the model (*26*).

Our spectroscopy measurements of finite chains also show how end effects can lower the energy of the filled states within the chains, which suggests a possible driving force for the formation of end states. For the four-atom and five-atom chains, the lowest three states are nearly degenerate in energy, with the end effects providing a substantial energy savings (0.4 eV for the filled states in the five-atom chain) when compared with models in which the end effects are omitted. Similar energy savings for the filled states are calculated for all of the chains studied. In contrast, this mechanism is not applicable to previously studied chain systems of Au on NiAl(110) and Cu on Cu(111), which have only empty states (*9*–*11*). The formation of end states does not lower the energy unless they are filled, possibly explaining why a particle-in-a-box model was sufficient in these previous studies. The formation of end states provides a mechanism, in addition to the Peierls distortion (*27*), to lower the total energy for 1D chains of finite length.

From the calculated DOS in the chains, we can model the constant-current STM profiles along the chains and thus verify the origins of the end effects seen at different bias voltages in Fig. 1. Figure 1, E and F, compares calculated and experimental profiles along a nine-atom chain for tunneling into the empty and filled states. The model uses the calculated DOS with the aforementioned parameters (*26*) along with a transmission function that describes the decay of the wave functions into the vacuum. We further assume a constant DOS for the tip and neglect tip convolution effects. The calculated constant-current profiles exhibit pronounced dips between atoms that are much weaker in the experiment because of the finite size of the tip. Nevertheless, the relative heights at the atomic position (filled circles in Fig. 1, E and F) are in fair agreement with the experiment, especially considering the simplicity of the model.

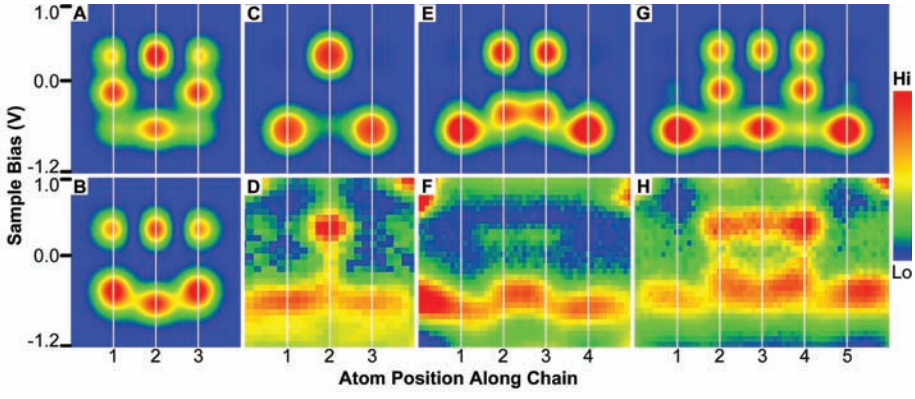

Fig. 3. Tight-binding calculations of the DOS and experimental differential conductance measurements as a function of bias voltage and position along the chain for three-, four- and five-atom chains. The magnitude of the differential conductance is represented on a rainbow color scale, with red as high intensity and blue as low intensity, and plotted as a function of position on the *x* axis and sample bias on the *y* axis. For the three-atom chain, different tight-binding parameters are tested (**A** to **C**) and are compared with an experimental *dI*/*dV* measurement taken with a constant-current set point (**D**). Only the model that includes end states (**C**) agrees with the experiment. The presence of end states is confirmed by extending the model to (**E**) four-atom and (**G**) five-atom chains, providing good agreement with the experimental *dI*/*dV* measurements in (**F**) and (**H**), respectively. The distance along the chains is measured in units of the Si lattice spacing along the chain direction (3.84 Å).

References and Notes

1. A. Zangwill, *Physics at Surfaces* (University Press, Cambridge, 1988).
2. S. G. Davison, M. Stęślicka, *Basic Theory of Surface States* (Oxford Univ. Press, New York, 1992).
3. M. V. Bollinger *et al.*, *Phys. Rev. Lett.* **87**, 196803 (2001).
4. L. Burgi, O. Jeandupeux, A. Hirstein, H. Brune, K. Kern, *Phys. Rev. Lett.* **81**, 5370 (1998).
5. M. F. Crommie, C. P. Lutz, D. M. Eigler, *Nature* **363**, 524 (1993).
6. Y. Hasegawa, P. Avouris, *Phys. Rev. Lett.* **71**, 1071 (1993).
7. J. Repp, G. Meyer, K. H. Rieder, *Phys. Rev. Lett.* **92**, 036803 (2004).
8. M. F. Crommie, C. P. Lutz, D. M. Eigler, *Science* **262**, 218 (1993).
9. N. Nilius, T. M. Wallis, W. Ho, *Science* **297**, 1853 (2002).
10. T. M. Wallis, N. Nilius, W. Ho, *Phys. Rev. Lett.* **89**, 236802 (2002).
11. S. Folsch, P. Hyldgaard, R. Koch, K. H. Ploog, *Phys. Rev. Lett.* **92**, 056803 (2004).
12. J. N. Crain *et al.*, *Phys. Rev. B* **69**, 125401 (2004).
13. J. R. Ahn, H. W. Yeom, H. S. Yoon, I. W. Lyo, *Phys. Rev. Lett.* **91**, 196403 (2003).
14. K. N. Altmann *et al.*, *Phys. Rev. B* **64**, 035406 (2001).
15. R. Losio *et al.*, *Phys. Rev. Lett.* **86**, 4632 (2001).
16. P. Segovia, D. Purdie, M. Hengsberger, Y. Baer, *Nature* **402**, 504 (1999).
17. An STS study of Si(111) 5×2-Au revealed 1D Schottky barriers between insulating and metallic chain segments.
18. H. S. Yoon, S. J. Park, J. E. Lee, C. N. Whang, I. W. Lyo, *Phys. Rev. Lett.* **92**, 096801 (2004).
19. J. N. Crain *et al.*, *Phys. Rev. Lett.* **90**, 176805 (2003).
20. J. R. Ahn, H. W. Yeom, H. S. Yoon, I. W. Lyo, *Phys. Rev. Lett.* **91**, 196403 (2003).
21. H. W. Yeom *et al.*, *Phys. Rev. Lett.* **82**, 4898 (1999).
22. M. M. J. Bischoff, T. Yamada, A. J. Quinn, H. van Kempen, *Surf. Sci.* **501**, 155 (2002).
23. Two caveats must be considered in interpreting any spatially resolved STS measurements. The DOS is convolved with the finite size of the tip leading to a spatial broadening. Also, a constant-current set point determines the tip-sample separation for each measurement, leading to an exponential increase in the differential conductivity when the tip-sample separation decreases, such as off the ends of the chains.
24. Choices with positive t_1 are ruled out from modeling longer chains.
25. J. N. Crain, D. T. Pierce, data not shown.
26. Consistency among different chain lengths requires the inclusion of (i) a nearest-neighbor hopping integral for the end atoms $t_{1\ end} = -0.19$ eV that is reduced as compared with the nearest-neighbor hopping integral between central atoms $t_1 = -0.34$ eV, (ii) a second-nearest-neighbor hopping integral of $t_2 = 0.10$ eV, and (iii) binding energies of $\varepsilon_1 = -0.60$ eV for the end atoms, $\varepsilon_2 = -0.09$ eV for the atoms second from the end, and $\varepsilon_0 = -0.27$ eV for the remaining atoms in the interior of the chain. For the four-atom chain there are no middle atoms, so only energies ε_1 and ε_2 are used.
27. R. F. Peierls, *Quantum Theory of Solids* (Clarendon, Oxford, 1955).

28. We thank M. D. Stiles for insightful discussions and suggestions concerning modeling, J. A. Stroscio for helpful discussions and for building the STM, R. J. Celotta and J. W. Gadzuk for helpful comments, and S. R. Blankenship for technical assistance. This work was supported in part by the Office of Naval Research.

29 October 2004; accepted 23 December 2004
10.1126/science.1106911

Photic Zone Euxinia During the Permian-Triassic Superanoxic Event

Kliti Grice,[1]* Changqun Cao,[2] Gordon D. Love,[3] Michael E. Böttcher,[4] Richard J. Twitchett,[5] Emmanuelle Grosjean,[3] Roger E. Summons,[3] Steven C. Turgeon,[6] William Dunning,[1] Yugan Jin[2]

Carbon and sulfur isotopic data, together with biomarker and iron speciation analyses of the Hovea-3 core that was drilled in the Perth Basin, Western Australia, indicate that euxinic conditions prevailed in the paleowater column during the Permian-Triassic superanoxic event. Biomarkers diagnostic for anoxygenic photosynthesis by Chlorobiaceae are particularly abundant at the boundary and into the Early Triassic. Similar conditions prevailed in the contemporaneous seas off South China. Our evidence for widespread photic-zone euxinic conditions suggests that sulfide toxicity was a driver of the extinction and a factor in the protracted recovery.

The most severe extinction of the past 500 million years occurred in the Late Permian (*1*, *2*). The biotic crisis was accompanied by an oceanic anoxic event (OAE) that may have lasted up to 8 million years. Although different authors report various anoxic intervals, the most severe conditions persisted during the first 1 to 3 million years (*3*, *4*). Anoxia has been proposed to have had a major role in driving the extinction (*5*, *6*); surface outcropping of sulfidic waters and emissions of hydrogen sulfide to the atmosphere provide a kill mechanism that might account for the terrestrial and marine extinctions (*7*).

In anoxic zones of modern-day stratified lakes or restricted marine environments (e.g., the Black Sea and Antarctic fjords), conditions are favorable for bacterial reduction of sulfate to sulfide (e.g., *8*). Chlorobiaceae (green sulfur bacteria) are typical of these environments in which hydrogen sulfide extends into the photic zone, where it serves as the electron donor required for anoxygenic photosynthesis. Chlorobiaceae use a distinct assemblage of light-harvesting pigments comprising bacteriochlorophylls *c*, *d*, and *e* and the carotenoids isorenieratene and chlorobactene. Identification of these compounds, or their diagenetic alteration products, in sediments provides unequivocal evidence for photic zone euxinic (PZE) conditions in the past (e.g., *9*–*12*).

Here, we use carbon and sulfur isotopic data and biomarker and iron speciation analyses in a drill core (Hovea-3) from the onshore Perth Basin, Western Australia (*13*), to establish the redox conditions in the water column of the southern Tethys Ocean during the Permian-Triassic (P-T) superanoxic event. Biomarkers diagnostic for anoxygenic photosynthesis by Chlorobiaceae were identified in P-T boundary sediments of the organic-matter (OM)–rich Hovea-3 core and in coeval samples from the OM-lean Meishan-1, a new core drilled at the type section of Meishan, South China (fig. S1); these biomarkers demonstrate that waters of the Tethys Ocean were periodically euxinic in the photic zone during and after the extinction event.

Changhsingian and Griesbachian sediment samples of Hovea-3 (1960- to 1995-m depth) contain C_{18} and C_{19} aryl isoprenoids (Figs. 1A and 2A), and the Griesbachian sediments contain isorenieratane, the C_{40} parent hydrocarbon (Figs. 1A and 2B and fig. S2). Highly specific bacteriochlorophylls can also give rise to distinctive maleimides (*9*). Methyl *iso*-butyl maleimide was identified in the polar fractions [see (*13*) for separation of maleimides]. The highest concentrations of all these pigment derivatives are preserved in the Griesbachian, reflecting high green sulfur bacterial activity and, thus, PZE conditions. Isorenieratane and aryl isoprenoids (including low pristane/phytane ratios) also occur in the latest Changhsingian and earliest Induan (Griesbachian) sediments (beds 22 to 27) of the global boundary stratotype section and point (GSSP) at Meishan, South China, which suggests that PZE conditions were widespread (Fig. 1B and Fig. 3).

Although the above data provide evidence for PZE during the P-T transition, the presence of benthic epifaunal macroinvertebrates such as *Claraia* and spirorbids dem-

[1]Curtin University of Technology, Perth, Australia. [2]Nanjing Institute of Geology and Palaeontology, Nanjing, China. [3]Massachusetts Institute of Technology, Cambridge, MA 02139, USA. [4]Max Planck Institute for Marine Microbiology, Bremen, Germany. [5]Plymouth University, Plymouth, UK. [6]Oak Ridge National Laboratory, Oak Ridge, TN 37831, USA.

*To whom correspondence should be addressed. E-mail: K.Grice@curtin.edu.au

End States in One-Dimensional Atom Chains
J. N. Crain and D. T. Pierce (February 3, 2005)
Science **307** (5710), 703-706. [doi: 10.1126/science.1106911]

Editor's Summary

Science (print ISSN 0036-8075; online ISSN 1095-9203) is published weekly, except the last week in December, by the American Association for the Advancement of Science, 1200 New York Avenue NW, Washington, DC 20005.